nature photonics

Article

https://doi.org/10.1038/s41566-026-01868-5

# Monolithic integration of continuous-variable cluster-state generation, manipulation and measurement

Received: 17 July 2024

Accepted: 9 February 2026

Published online: 13 March 2026

Check for updates

Xinyu Jia[1,2,8] ✉, Chang You[1,8], Chonghao Zhai[1,8], Xuezhi Zhu[3], Yun Zheng[1], Tianxiang Dai[1], Zhaorong Fu[1], Xiaolong Su[3,4] ✉, Qihuang Gong[1,4,5,6] & Jianwei Wang[1,4,5,6,7] ✉

Photonic integrated circuits provide a controllable and scalable platform for quantum information processing. In particular, continuous-variable integrated photonic quantum devices—which encode quantum information in the quadratures of optical qumodes—provide distinct advantages, although generating multimode entanglement in such systems has remained a key challenge. Here we demonstrate a monolithic integrated quantum photonic circuit that enables the full on-chip generation, manipulation and measurement of continuous-variable multi-qumode cluster-state entanglement. The device incorporates strongly squeezed quantum light sources with wafer-scale scalability, high-fidelity single-qumode and two-qumode entangling gates, and local oscillators and interferometers for balanced homodyne detection—all on a single chip. This co-integration enables the preparation, control and measurement of four-qumode cluster states and individual qumodes with high stability and high fidelity. The monolithic integration of high-performance devices allows rigorous verification of genuine multipartite entanglement with unambiguous cluster-state structures. This work establishes a controllable and scalable platform for optical quantum computing, networking and sensing.

In recent decades, substantial advances have been made in the development of quantum computational devices[1–4]. The quest for large-scale quantum computing demands devices with both high scalability and high controllability. This entails the capacity to scale up the number of quantum bits or modes (that is, qubits or qumodes) that are coherently entangled, and the capacity to encode, process and read out quantum information with exceptional precision at the individual qubit or qumode level. Optical quantum devices, known for long coherence times and low noise at room temperature, present one compelling avenue for quantum computation and information processing[5]. The realization of universal optical quantum computation hinges on executing a sequence of precise measurements and feed-forward operations on individual qubits or qumodes of cluster states[6,7]. Substantial progress has been made in the deterministic generation of large-scale cluster states through encoding qumodes in the continuous quadratures of light fields[8], leveraging various degrees of freedom of light in bulk and fibre optic systems[9–14].

[1]State Key Laboratory for Mesoscopic Physics, School of Physics, Peking University, Beijing, China. [2]Beijing Academy of Quantum Information Sciences, Beijing, China. [3]State Key Laboratory of Quantum Optics and Quantum Optics Devices, Institute of Opto-Electronics, Shanxi University, Taiyuan, China. [4]Collaborative Innovation Center of Extreme Optics, Shanxi University, Taiyuan, China. [5]Frontiers Science Center for Nano-optoelectronics and Collaborative Innovation Center of Quantum Matter, Peking University, Beijing, China. [6]Hefei National Laboratory, Hefei, China. [7]Beijing Key Laboratory of Advanced Micro- and Nanoscale Light Source Materials and Devices, Peking University, Beijing, China. [8]These authors contributed equally: Xinyu Jia, Chang You, Chonghao Zhai. ✉e-mail: xinyu.jia@pku.edu.cn; suxl@sxu.edu.cn; jww@pku.edu.cn

https://doi.org/10.1038/s41566-026-01868-5

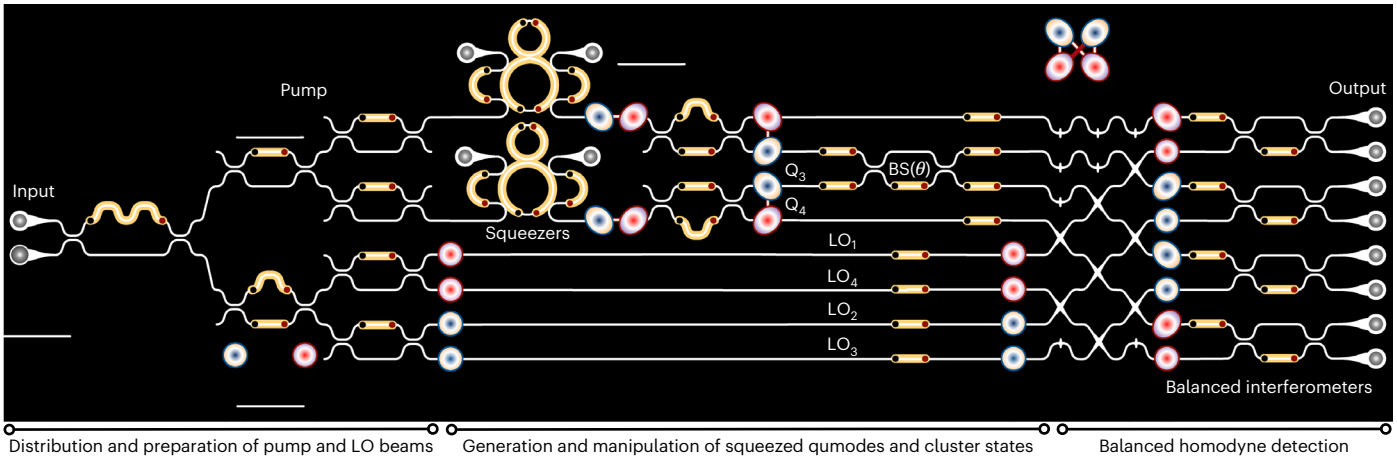


**Fig. 1 | Monolithic integrated CV-QPIC for the generation, manipulation and measurement of multi-qumode cluster states on a chip.** The CV-QPIC is fabricated on ultra-low-loss silicon nitride waveguides with a typical thickness of 800 nm and a typical width of 1 μm. There are three regions of the chip: distribution and preparation of the pump-LO beams (left), generation and operation of squeezed states and cluster states (middle) and balanced interference of squeezed LO beams for homodyne detection (right). Coloured pulses indicate the pump (green), LOs (solid red and blue) and squeezed (dotted red and blue) beams. The pump-LO beams are wavelength demultiplexed by asymmetric MZIs, and their power distribution into squeezers is controlled by cascaded MZIs, enabling high-quantity generation (by shaping the pump) and detection (by shaping the LO) of cluster states. Quadrature squeezed beams, such as two-qumode non-degenerate EPR states (featuring strong squeezing and a tunable spectrum) are deterministically generated at the two DMDI squeezers. Two qumodes (blue) of the EPR pairs meet and interfere at the reconfigurable MZI that acts as the two-qumode BS deterministic entangling gate. Single-qumode rotational gates are implemented by phase-shifters $R\{\theta_2', \theta_3', \theta_1, \theta_2, \theta_3, \theta_4\}$–. The quadrature of each qumode is measured by implementing balanced homodyne detection using the arrayed MZIs (precise combinations of each qumode and its LO) and reprogramming the measurement basis by the arrayed LO phase-shifters $\{\phi_1, \phi_2, \phi_3, \phi_4\}$ (the co-integration enables precise and stable control of the phase between each qumode and its LO). That is, the monolithic integrated circuit enables the preparation, control and measurement of individual qumode and cluster states with high phase stability and gate fidelity. Trichromatic pump-LO beams were prepared by electro-optic modulation and input into the chip via an optical fibre. An array of photodiodes with 95% efficiency was used for detection. The inset is an optical microscope image of one fabricated CV-QPIC chip on a 6-inch silicon nitride wafer. λ-demulti, demultiplexing of different wavelengths; Q1–Q4, quantum mode 1–4; LO, local oscillator 1–4.

An emerging technology in quantum photonic integrated circuits (QPICs) enables on-chip encoding, processing and readout of quantum information, marking a new era in large-scale quantum computation and information processing[15,16]. Previous research has predominantly focused on discrete-variable (DV)-QPICs, with the aim of generating, processing and detecting single-photon[17–19] and entangled qubits[20–24] on chip, and implementing quantum computing algorithms and quantum networking protocols[25–28]. Meanwhile, by guiding and operating continuous-variable (CV) qumodes in optical waveguide circuits, there is substantial potential to achieve exceptional phase stability, precise mode matching, low interface loss and high operation fidelity throughout the QPIC. Recent advances have enabled demonstrations of integrated single-qumode and two-qumode squeezed light sources[29–38], and realizations of Gaussian boson sampling (a type of special-purpose quantum computing) by adopting several of these squeezed sources[26,39,40]. Very recently, remarkable progress has been made in the deterministic generation of multi-qumode cluster-state entanglement on chip in a frequency-multiplexed microcomb[41] and a time-multiplexed chip–fibre-interconnected phase-locked system[42], for example. However, formidable challenges remain in realizing a monolithic integrated CV-QPIC that is capable of generating, manipulating and measuring cluster states—the key resource for universal quantum computing[5–7]. Addressing the challenge of monolithic integration is essential to fully leverage the scalability and controllability of CV-QPICs.

In this work we demonstrate a monolithic integrated CV-QPIC that is capable of generating, manipulating and measuring multi-qumode entangled cluster states and individual qumodes encoded in the spatial (path) modes, achieving excellent controllability and scalability. A full spectrum of key devices has been monolithically integrated, including strongly squeezed light sources with strong spectral tunability, reconfigurable linear optics for single-qumode gates and two-qumode beam splitter (BS) deterministic entangling gates, and local oscillators and balanced interferometers for homodyne detection. The co-integration of all key devices enables the phase-stable, high-fidelity operation of qumodes, as demonstrated through hour-long quadrature measurements (without active phase locking) and the achievement of over 99.9% fidelity for both single-qumode and two-qumode quantum gates. All of these devices are fabricated on a silicon nitride platform through wafer-scale photolithography, enabling mass manufacturing and large-scale integration while maintaining high performance—for example, the squeezers can be precisely controlled to achieve uniform spectral profiles across a 6-inch wafer, promising large-scale entanglement generation with scalable control and compatibility with mass manufacturing. We successfully validate multipartite entanglement in the four-qumode cluster state through the violation of van Loock–Furusawa inequalities and full characterization of the nullifier covariance matrix, underscoring the transformative potential of this CV-QPIC technology.

Figure 1 shows a diagram of the CV-QPIC, which can generate, manipulate and measure path-encoded four-mode non-degenerate cluster states. It is fabricated on an ultra-low-loss (0.1dB cm−1) silicon nitride platform[43]. The chip includes three main parts with different functions: (1) the distribution and preparation of pump-local oscillator (LO) beams; (2) the generation of squeezed states and cluster states; and (3) the balanced interference of squeezed LO beams for homodyne detection of cluster states. A diagram of the experimental set-up is provided in Supplementary Fig. 1. Phase-locked pump-LO trichromatic beams are input into the quantum chip via a fibre. Homodyne detection is closed by an array of eight photodiodes after the chip. Pump-LO beams with different wavelengths are demultiplexed using an asymmetric Mach–Zehnder interferometer (MZI). Cascaded MZIs are used to split and balance power for the squeezer pumps. Similarly, four LOs are prepared and individually tailored, enabling full control

https://doi.org/10.1038/s41566-026-01868-5

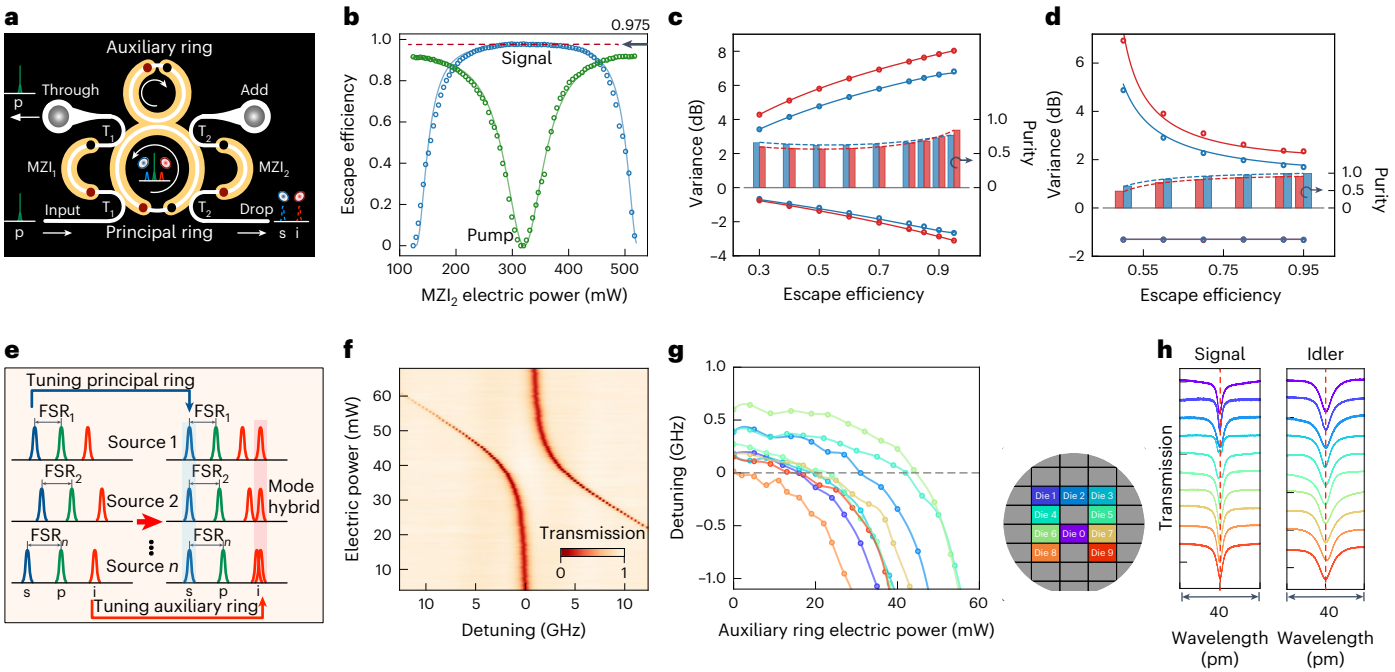


**Fig. 2 | Characterizations of integrated squeezed light sources with strong squeezing, high tunability and high purity. a**, Diagram of the DMDI squeezing sources. By controlling the two asymmetric MZIs ($MZI_1$ and $MZI_2$), the pump (p) is critically coupled out at the through port, while the generated squeezed signal (s) and idler (i) beams are optimally coupled out at the drop port. By independently controlling the two microrings, the wavelengths of the s and i squeezed beams can be precisely tuned. $T_1$ and $T_2$ (where $T_1 < T_2$) are the transmissivities of the beam splitters that form $MZI_1$ and $MZI_2$, respectively. **b**, The escape efficiencies of the $\lambda_p$ and $\lambda_s$ modes can be controlled by tuning the power applied to $MZI_2$ (with $MZI_1$ preset at its optimal configuration). Data points represent experimental data and solid lines are theoretically calculated results from the model in Supplementary Section 2.1. Red dashed line and blue arrow indicate a maximum escape efficiency of 0.975. **c**,**d**, Measured and theoretical squeezing (bottom) and anti-squeezing (top) variances and on-chip state purity for single-mode squeezing (blue) and two-mode squeezing (red). The data points and bars represent experimental data and the solid and dashed lines represent theoretical results based on the quantum optical field evolution model in Supplementary Section 2.2. **c**, The escape efficiency was varied under constant pump power (normalized to the optical parametric oscillation threshold). **d**, The escape efficiency was adjusted while maintaining fixed on-chip squeezing at −2.5 dB (key for non-Gaussian state generation). **e**, Schematic of spectral tuning for the squeezed beam wavelengths. The spectral distributions of signal ($\lambda_s$) and idler ($\lambda_i$) squeezed qumodes can be independently aligned by tuning the principal and auxiliary microrings, respectively. Fabrication-induced inhomogeneities in the free spectral range (FSR) (dispersion) can be compensated post-fabrication by mode hybridization between these two microrings. **f**, Experimental mode hybridization at the $\lambda_s$ mode through tuning of the auxiliary microring, showing a 6 GHz mode splitting. Colour represents normalized transmission. **g**,**h**, Demonstration of wafer-scale spectral tuning of DMDI squeezers. Ten squeezers distributed across multiple dies on a 6-inch silicon nitride wafer (inset) were characterized to verify their wavelength tuning and qumode alignment capability. Signal modes ($\lambda_s$) were aligned by tuning the principal microrings, followed by alignment of the idler modes ($\lambda_i$) by tuning the auxiliary ring. **g**, The idler frequencies of nine squeezers were finely tuned to match that of the reference squeezer on die 0 (dashed line). Data points represent experimental data of detuning to reference squeezer (die 0) when auxiliary rings are tuned. **h**, The spectra of all ten squeezers were precisely aligned to the die 0 squeezer, as indicated by the dashed red lines. Left (Right) panel: transmission around the signal (idler) frequency. For the experiments shown in **f**–**h**, $MZI_1$ was set at the optimal configuration and $MZI_2$ was tuned such that the signal mode was critically coupled.

of the intensities for precise quadrature measurement. Two pairs of two-qumode non-degenerate Einstein–Podolsky–Rosen (EPR) states are created at two quadrature squeezed sources, and four-qumode cluster states are generated via the interference of two qumodes of the EPR pairs at a reconfigurable beam splitter (that is, a MZI). We devised a dressed photonic molecule configuration for the squeezers, which enables fine-tuning of the squeezing strength and the wavelength of the qumodes. Single-qumode rotational gates are implemented with reconfigurable phase-shifters, and deterministic entangling gates are realized at the integrated beam splitter. The generation and entanglement of qumodes are both deterministic. The quadrature measurements for each qumode is implemented via balanced homodyne detections at the MZIs that precisely combine each qumode with its LO, with the measurement bases defined by on-chip phase-shifters $\phi_i$ that precisely set the phase between each qumode and its LO. Monolithic integration of these devices achieves a total loss of ~1.8–2.6 dB, suppresses high-order modes without requiring mode cleaning (Supplementary Section 1) and realizes exceptional phase stability and gate fidelity without active phase locking (Fig. 3).

## Characterization of quadrature squeezers

Figure 2a shows a schematic of the squeezer, which has a 'penguin-shaped' dual-microring dual-interferometer (DMDI) configuration. A quadrature squeezed vacuum can be generated by using the enhanced spontaneous four-wave-mixing (FWM) process in the high-quality-factor ($Q$) silicon nitride microring resonator, operating below the threshold of optical parametric oscillation. This design of the DMDI configuration simultaneously allows strong squeezing and high state purity via individual control of the coupling of the pump and squeezed modes at two asymmetric MZI couplers[44,45] and tuning of the wavelength of the squeezed mode through tailoring of the local dispersion of a principal microring coupled to an auxiliary microring[46,47]. The DMDI can be fully described by the transfer matrix formalism (Supplementary Section 2). Single-mode and two-mode squeezing states are generated by degenerate and non-degenerate spontaneous FWM processes.

The dual-interferometer structure consists of $MZI_1$ and $MZI_2$, which serve as the input for the pump and the output for squeezed light. These asymmetric MZIs have a free spectral range that is twice that of the

https://doi.org/10.1038/s41566-026-01868-5

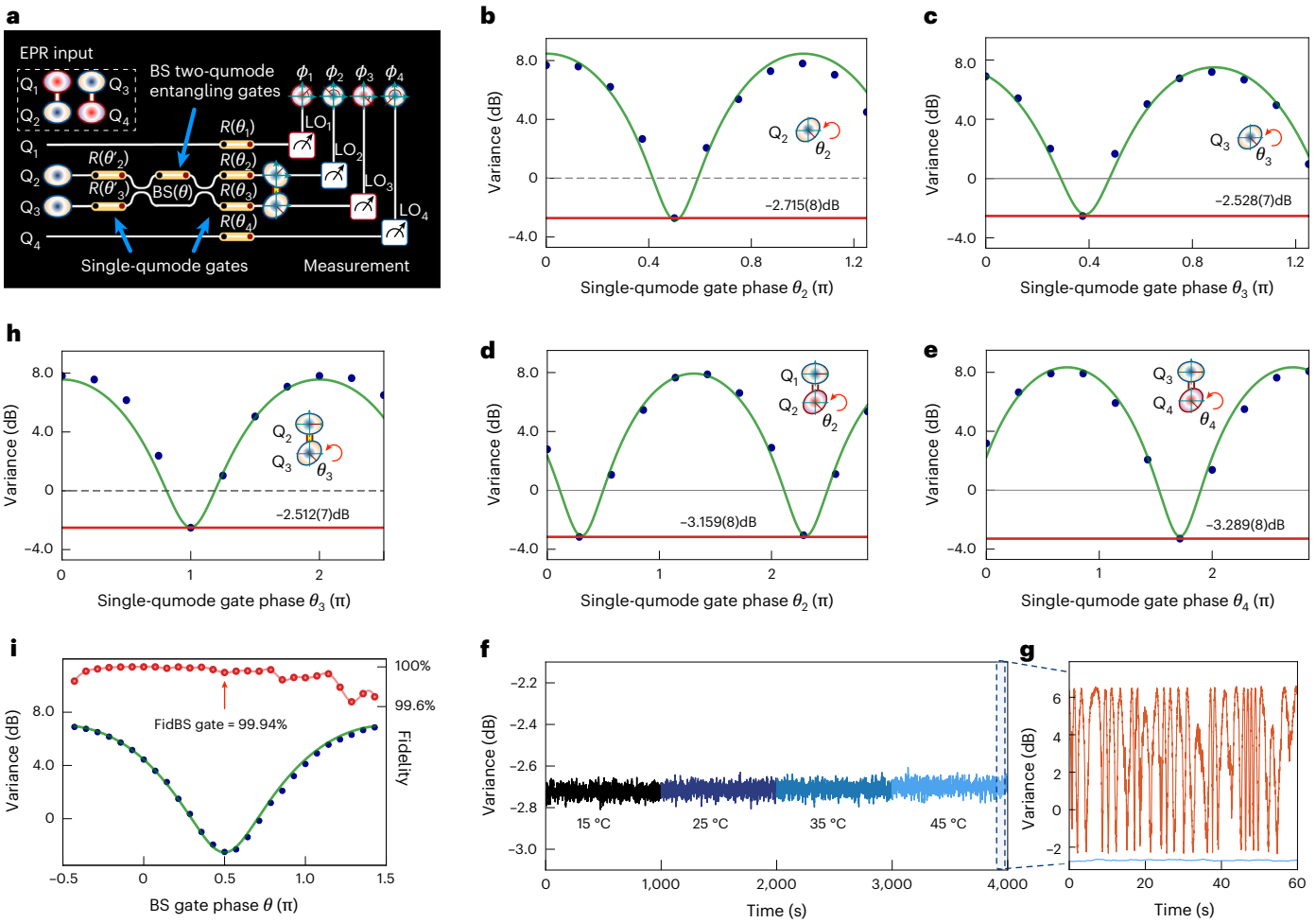


**Fig. 3 | Characterizations of integrated single-qumode rotational gates and two-qumode BS entangling gates. a**, Simplified circuit diagram highlighting the single-qumode rotation gates ($R(\theta_i)$), two-qumode BS entangling gate (BS($\theta$)) and LO$_i$ projectors. Two-mode degenerate EPR states are created through the interference of $\hat{x}$-squeezed and $\hat{p}$-squeezed qumodes at the integrated beam splitter, which is implemented by precisely reconfiguring the MZI into a balanced configuration and serves as a deterministic two-qumode BS entangling gate. **b**–**e**, Experimental manipulation and measurement of single-mode degenerate squeezed states from squeezers 1 (**b**) and 2 (**c**) and two-mode non-degenerate squeezed states from squeezers 1 (**d**) and 2 (**e**). Data points represent the measured quadrature variances obtained while operating the single-qumode rotation gates $R(\theta_i)$ and green lines show the theoretical predictions based on a quantum-field-evolution model. Grey dashed lines indicate the shot-noise-level reference. Strong squeezing of −2.715 dB (single-mode) and −3.289 dB (two-mode) was measured (indicated by red lines) when the escape efficiency was 0.95. Insets: schematics of single-mode and two-mode squeezed states, with circular arrows indicating the qumodes that are rotated during measurements. **f**, Characterizations of the on-chip phase stability and single-qumode rotation gates. Quadrature squeezing was measured over 1 h at fixed on-chip phases, without external phase locking, and repeated at different chip temperatures (with squeezers relocked and the chip realigned to ensure consistency). The results demonstrate high phase stability, with the quadrature variance showing a standard deviation of 0.02 dB, corresponding to a phase fluctuation below 0.3°. The single-qumode rotation gate fidelity is estimated to be Fid$_{\text{rotation gate}}$ = 99.92%. **g**, Measurements of the same state using off-chip fibre-based homodyne interferometers, exhibiting pronounced phase drift in the absence of active phase stabilization. For comparison, a segment of data in **f** is also shown by blue line. **h**,**i**, Characterizations of the two-qumode BS entangling gates, with an input of the two squeezers in **b** and **c** with pre-aligned spectra. **h**, The variance of noises for the generated two-mode non-degenerate EPR states measured when $\theta_{BS} = \pi/2$, showing a strong squeezing of −2.512 dB that approaches the two single-mode squeezing in **b** and **c**. Inset: schematic of the EPR pair, with circular arrow indicating the rotated qumode during measurement. **i**, Bottom: the variance of $(\hat{p}_2 - \hat{p}_3)$ was measured while sweeping the phase $\theta_{BS}$ (blue data points), from which the actual BS gate phase could be extracted. The green line shows the theoretically calculated variance for different $\theta_{BS}$, given the two input squeezed modes. Top: measured fidelities for general two-mode operations (red data points). The BS gate fidelity was estimated to be Fid$_{\text{BS gate}}$ = 99.94% when $\theta_{BS} = \pi/2$. Note that the phases of the maximally squeezed and anti-squeezed quadratures differ by π/2 in **b** and **c**, whereas in **d**, **e** and **h** scanning the phase of one qumode reveals a phase disparity of π between the maximally squeezed and anti-squeezed quadratures. Values in the bottom right of **b**–**e** and **h** are measured squeezing degrees, and values in parentheses are ±1$\sigma$ uncertainty estimated from a full set of 400 data points. All experimental data were collected at a 5 MHz sideband frequency.

principal microring (200 GHz). Their effective coupling to the microring ($T_{\text{eff}}$) can be precisely controlled (Supplementary Information). The key to achieving strong squeezing lies in maintaining continuous circulation of the pump within the microring, and efficiently extracting the created signal and idler squeezing beams out of the microring (see the measured transmission spectra in Supplementary Fig. 4). Through tailoring MZI$_{1,2}$, fully dynamic control of the escape efficiency up to 0.975 at the drop port was obtained in the experiments, as shown in Fig. 2b. The $Q$ value can be further dynamically steered by tuning the MZI$_2$ (Supplementary Fig. 3), so the escape efficiency can be optimized to generate strongly squeezed single-mode and two-mode states.

The dual-microring configuration consists of two rings with a ratio of 3:4 in their free spectral ranges. The two microrings can be closely controlled to compensate the wavelength inhomogeneity between

**Table 1 | Comparison of state-of-the-art CV-QPICs**

| CV-QPIC | Platform | Squeezer | Monolithic integration | Phase locking | Entanglement verification |
|---|---|---|---|---|---|
| Two-mode squeezing[32] | $SiO_2$ | – | Gate, BHD MZI | Required | Inseparability criterion |
| Two-mode squeezing[37] | $SiO_2$ | 1.6(3.1) dB, $\bar{T}$ | Squeezer | Required | – |
| Two-mode squeezing[33] | LN | 1.4(3.0) dB, $\bar{T}$ | Squeezer, gate, BHD MZI | Required | Inseparability criterion |
| Single-mode squeezing[30] | LNOI | 4.2(10) dB, $\bar{T}$ | Squeezer | Required | – |
| Single-mode squeezing[31] | LNOI | 0.12(0.6) dB, $\bar{T}$ | Squeezer, gate, BHD MZI | Required | – |
| Homodyne detection[56] | Si | – | BHD | Required | – |
| Gottesman–Kitaev–Preskill qubit[54] | $Si_3N_4$ | 5.2(10) dB, T | Squeezer, boson sampling | Required | – |
| Eight-mode frequency cluster[41] | $Si_3N_4$ | 2.1(6.0) dB, $\bar{T}$ | Squeezer | Required | vLF inequalities, Null. mat., PPT |
| $10^{10}$-mode path-time cluster[42] | $Si_3N_4$ | 0.13(4.0) dB, T | Chip–fibre connected system | Required | only Nullifier measurement |
| Four-mode path cluster (this work) | $Si_3N_4$ | 3.2(9.7) dB, $\bar{T}$ | Squeezer, gate, BHD MZI, LO | Not required, stable | vLF inequalities, Null. mat., PPT |

The CV-QPIC platforms include silica ($SiO_2$), lithium niobate (LN), lithium niobate on insulator (LNOI), silicon on insulator (SOI) and silicon nitride ($Si_3N_4$). Values outside parentheses in the ÏSqueezers' column indicate squeezing levels measured off chip; values inside parentheses represent inferred on-chip squeezing. T denotes spectrally tunable squeezers; $\bar{T}$ denotes non-tunable squeezers and T denotes spectral tunability demonstrated at the wafer scale. Monolithic integration refers to the co-integration of key components on a single chip, including squeezers, single- and two-mode gates, balanced homodyne detection (BHD), MZIs for BHD and LOs. The phase locking column indicates the use of active phase stabilization to ensure the high-fidelity operation and measurement of qumodes and entangled states. In this work, monolithic integration enables intrinsic phase stability without active locking. Entanglement verification methods include the violation of two-mode inseparability criteria or van Loock–Furusawa (vLF) inequalities for multimode Gaussian states (vLF inequalities), reconstruction of the nullifier covariance matrix (Null. mat.) and violation of the positive partial transpose (PPT) criterion.

different squeezers due to fabrication disorders. Following fine-tuning of the resonance of the auxiliary microring to match that of the principal microring, the two resonant modes become degenerate and mode splitting occurs[46,47], akin to the energy level hybridization in molecules. As depicted in Fig. 2e, the wavelength for the squeezed modes ($\lambda_s$) can be adjusted by simply tuning the principal microring, and subsequently the optimal alignment between the $\lambda_i$ squeezed modes can be achieved by tuning the auxiliary microring to induce mode splitting. The experimental result presented in Fig. 2f demonstrates the mode hybridization, featuring a splitting strength of ~6 GHz that was adequate in our experiments. Such delicate spectral engineering of squeezers is crucial, as it enables excellent spectral alignment and interference between distinct squeezers at different locations on the chip, and eventually leads to high-fidelity multi-qumode entanglement. We then characterized the wavelength tuning and qumode alignment capability for both $\lambda_s$ and $\lambda_i$ squeezed modes using ten DMDI sources distributed across different dies fabricated on a 6-inch wafer. The tuning procedures for $\lambda_s$ and $\lambda_i$ modes were implemented independently. As shown in Fig. 2g, after pre-aligning all ten signal modes by tuning the principal microrings, the idler modes exhibited marked spectral misalignment. Subsequent adjustment of the auxiliary rings enabled precise alignment of each squeezer's idler mode to the reference device (die 0). The resulting spectral distribution of all ten squeezed mode pairs (Fig. 2h) confirms wafer-scale spectral tunability—a crucial requirement for scaling cluster-state entanglement.

Single-mode and two-mode squeezed states were generated at the DMDI sources through degenerate and non-degenerate spontaneous FWM. We characterized the quadrature variance by scanning the phases LO $\phi_i$ or gate $\theta_i$ (see labels in Figs. 1 or 3a), and (anti-)squeezing variance can be precisely read out at certain phases. The phase settings of $\phi_i$ of LOs define the measurement basis for each individual qumode. Each qumode meets with its LO at a balanced MZI for homodyne detections. An array of fibre-coupled photodiodes was used for detections (see the experimental set-up in Supplementary Fig. 1). The variance of the noise levels was recorded by a spectrum analyser at a sideband frequency of 5 MHz. Figure 3b–e reports the measured quadrature variances for single-mode and two-mode squeezers.

The degree of squeezing can be fully steered in squeezers. Tuning the dual MZIs results in a substantial enhancement of squeezing. Figure 2c shows measured squeezing strengths of −2.715 dB for single-mode squeezers and −3.289 dB for two-mode squeezers. Their corresponding quadrature variances are plotted in Fig. 3b–e. After accounting for device and set-up losses (see Supplementary Section 1), the inferred on-chip squeezing levels were estimated to be −7.515 dB for single-mode squeezing and −9.732 dB for two-mode squeezing. The results of the strong squeezing level and wafer-scale spectral tunability thus demonstrate the superiority of our DMDI squeezers (a comparison of integrated squeezers is presented in Table 1).

## Qumode manipulation via single-qumode and two-qumode gates

As depicted in Fig. 3a, the $R(\theta_i)$ gates in the CV-QPIC act as single-qumode rotational gates for individual squeezed qumodes $Q_i$. The quadrature variance results in Fig. 3b–e indicate the stable and precise on-chip operation and measurement of qumodes. To quantitatively characterize these gates, we performed continuous quadrature measurements over 1 h, without active phase stabilization and locking. Experimental results are reported in Fig. 3f. Note that the on-chip phase was intentionally offset from the minimum of the variance–phase curve to allow quantification of phase fluctuations using variance changes. The measured quadrature variance showed a standard deviation of 0.02 dB over this period, corresponding to a phase fluctuation of 0.0015π (0.3°). The CV-QPIC consistently maintained phase stability under varying ambient temperatures (multicolour data in Fig. 3f). This result demonstrates high-precision rotation operation and measurement, giving rise to a single-qumode rotation gate fidelity of 99.92% (defined as $1-\frac{\Delta\theta}{2\pi}$, where $\Delta\theta$ represents phase fluctuation). In contrast, off-chip fibre-based homodyne interferometry exhibited strong phase drift under the same environmental conditions (Fig. 3g), underscoring the superior robustness of monolithic QPICs.

We then characterized the operational fidelity of the two-qumode BS deterministic entangling gate. This was implemented by interfering an $\hat{x}$-squeezed qumode and a $\hat{p}$-squeezed qumode generated by two separate sources at a 50:50 integrated beam splitter, which is implemented by reconfiguring the MZI as a balanced BS, as shown schematically in Fig. 3a. Before interference, both squeezers were spectrally aligned to the same wavelength (Fig. 2g,h), and their quadrature orientations were preset by operating single-mode rotation gates $R(\theta'_{2,3})$. To evaluate the quantum performance of the BS gate, we measured the variance of $(\hat{p}_2-\hat{p}_3)$ between qumodes Q2 and Q3 while varying the phase $\theta_{BS}$ (results in Fig. 3i). As the MZI precisely implements the BS entangling gate ($\theta_{BS}=\pi/2$), it produces the two-mode degenerate

**Table 2 | Experimental van Loock–Furusawa values**

| Forms of van Loock-Furusawa criterion | Measured van Loock–Furusawa value |
|---|---|
| $\left\langle(\Delta\hat{N}_1)^2\right\rangle+\left\langle(\Delta\hat{N}_2)^2\right\rangle$ | 1.964 ± 0.009 |
| $\left\langle(\Delta\hat{N}_2)^2\right\rangle+\left\langle(\Delta\hat{N}_3)^2\right\rangle$ | 1.956 ± 0.010 |
| $\left\langle(\Delta\hat{N}_3)^2\right\rangle+\left\langle(\Delta\hat{N}_4)^2\right\rangle$ | 1.930 ± 0.114 |
| $\left\langle(\Delta\hat{N}_4)^2\right\rangle+\left\langle(\Delta\hat{N}_1)^2\right\rangle$ | 1.939 ± 0.016 |

The values for different edges were obtained by summing the variances of the measured nullifiers. If the measured value is less than 2, the inequality is violated, and if the inequalities for all edges are violated, it suggests the presence of multipartite quantum entanglement in the cluster states. Values are listed with ±1σ uncertainties, each of which were estimated from a full set of 400 data points.

maximally entangled EPR state. The measured quadrature variance for this EPR state is reported in Fig. 3i. From these measurements, the BS gate fidelity can be quantified as 99.94%, along with the corresponding fidelities for general two-qumode Gaussian operations (red data points), where fidelity is defined as the Hilbert–Schmidt inner product $\left|\mathrm{Tr}(U_{\mathrm{th}}^{\dagger}U_{\mathrm{meas}})/2\right|$, where $U_{\mathrm{th}}$ and $U_{\mathrm{meas}}$ are theoretical and measured two-mode unitary matrices. Hence, the observation of −2.512 dB two-qumode degenerate squeezing in Fig. 3i signifies high-fidelity operation of single-qumode gates and a two-qumode entangling gate, as well as the high-level spectral identity of these DMDI squeezers.

## Generation and verification of cluster-state entanglement

We generated and verified a four-qumode box-type cluster state, which serves as a demonstration of the full range of capabilities realized on the monolithic CV-QPIC, including the high phase stability and operation fidelity. In this experiment, the two sources were operated with strong squeezing, and they were tailored to have closely matching wavelengths, resulting in the generation of two identical pairs of two-mode non-degenerate EPR states. Following switching at the entangling gate with $\theta_{\mathrm{BS}}=\pi/2$, a weighted box-type cluster state was deterministically generated that had three edges with weight $1/\sqrt{2}$ and one edge with weight $-1/\sqrt{2}$ (Supplementary Information). The circuit scheme is shown in Figs. 1 and 3a. The four-mode box cluster state can be described by its nullifiers $\hat{N}_i$, which are defined as follows:

$$\begin{aligned}\hat{N}_1&=\hat{p}_1+\tfrac{\hat{p}_2+\hat{p}_3}{\sqrt{2}},\ \hat{N}_2=\hat{x}_1-\tfrac{\hat{x}_2+\hat{x}_3}{\sqrt{2}},\\ \hat{N}_3&=\hat{p}_4+\tfrac{-\hat{p}_2+\hat{p}_3}{\sqrt{2}},\ \hat{N}_4=\hat{x}_4-\tfrac{-\hat{x}_2+\hat{x}_3}{\sqrt{2}},\end{aligned}\tag{1}$$

where $\hat{x}_i$ and $\hat{p}_i$ ($i\in[1,2,3,4]$) are the quadrature operators for the four qumodes. These nullifiers are equivalent to the commonly used ones $\hat{N}_i=\hat{p}_i-\sum_{j\in\mathcal{N}(i)}A_{ij}\hat{x}_j$ (where $\mathcal{N}(i)$ denotes the set of node $i$'s neighbours and $A_{ij}$ represents a adjacency matrix)[48], up to a local Fourier transform (that is, π/2 phase rotation) on half of the qumodes (Supplementary Information). This transformation does not alter the entanglement and computational properties of the cluster state. In experiments, any linear combination of quadrature operators $\hat{x}_i$, $\hat{p}_i$ (that is, $\hat{x}_i\cos\theta_i+\hat{p}_i\sin\theta_i$) can be directly measured by reconfiguring the LOs and homodyne interferometers, all co-integrated on the CV-QPIC chip. This is achieved by tailoring the four LOs to match the desired combination coefficients, precisely setting their phases $\theta_i$ and performing addition or subtraction of the photocurrents from four off-chip balanced homodyne detectors (see the experimental set-up in Supplementary Fig. 1). Given the high phase stability and gate fidelity achieved on the monolithic integrated chip, $\hat{N}_i$ can be measured with high precision, and the full covariance matrix of the state can be faithfully reconstructed.

Figure 4 reports the experimental results of the four nullifiers $\hat{N}_i$. The squeezing values of four nullifiers were measured as being {−3.095dB, −3.079dB, −3.134dB, −3.194dB}. The nullifiers were measured with vacuum states used as the input reference (grey lines in Fig. 4a–d). The observation of stable nullifier variance once again demonstrates the exceptional phase stability and precision of the device.

We verified the inseparability of the generated cluster state by experimental violations of the van Loock–Furusawa inequalities[49]. A sufficient condition for determining the separability of the four-mode box cluster state is provided by the following inequality (Supplementary Information):

$$\left\langle(\Delta\hat{N}_i)^2\right\rangle+\left\langle(\Delta\hat{N}_j)^2\right\rangle\geq 2,\tag{2}$$

where $(i,j)=\{(1,2),(2,3),(3,4),(1,4)\}$, and $\hbar=2$ is chosen here (Supplementary Information), such that for a single-mode vacuum, $\langle(\Delta\hat{x}_{\mathrm{vac}})^2\rangle=\langle(\Delta\hat{p}_{\mathrm{vac}})^2\rangle=1$. The nullifier values, which were experimentally recorded in decibels using a spectrum analyser, are converted to linear units via the relation $\epsilon\cdot10^{\mathrm{dB}/10}$ (where the factor $\epsilon=2$ corresponds to nullifier variances when all qumodes are in a vacuum, accounting for the specific entanglement structure of the weighted box-type cluster state), enabling direct experimental quantification of the violation of the inequalities in equation (2). Table 2 summarizes the experimental violations of all four van Loock–Furusawa inequalities, successfully demonstrating the genuine multipartite entanglement in the generated CV cluster state.

To fully characterize the entanglement structure of the generated cluster state, we performed Gaussian state tomography to reconstruct its complete quadrature covariance matrix (see details in Supplementary Section 4.3). The reconstructed covariance matrix is presented in Fig. 4e. From this matrix, we further derived the nullifier correlation matrix, as shown in Fig. 4f. The diagonal elements, which represent the variances of individual nullifiers, exhibit excellent consistency with the directly measured values in Fig. 4a–d, with all values violating the van Loock–Furusawa criteria. The minimal off-diagonal elements rigorously certify the unambiguous box-type cluster-state entanglement structure. These experimental results are in excellent agreement with theoretical predictions (Supplementary Fig. 7). Furthermore, we verified the multimode inseparability through violation of the positive partial transpose criterion: a quantum state is inseparable under a given bipartition if the partially transposed density operator's covariance matrix has a symplectic eigenvalue smaller than one[50]. As shown in Fig. 4g, the cluster state consistently demonstrated inseparability across all seven bipartitions of the four qumodes, confirming genuine multipartite entanglement.

We also evaluated the robustness of the entanglement of the integrated photonic CV cluster states. Controlled phase offsets were intentionally introduced to the four rotation gates $R(\theta_i)$, and the corresponding nullifier quadratures were measured. As shown in Fig. 4h, while the entanglement structure shows sensitivity to phase variations, the violation of the van Loock–Furusawa criteria persists within a phase deviation tolerance of approximately 0.05π (9°)—substantially larger than the on-chip phase fluctuation of 0.3° observed in Fig. 3f. The full dataset is provided in Supplementary Fig. 6. These results therefore demonstrate the strong robustness of cluster-state entanglement in monolithically integrated CV-QPICs.

## Generation of squeezed pure states

For cluster state generation, the DMDI sources were configured to produce strongly squeezed modes (−3.2 dB two-mode squeezing) at the cost of reduced state purity (0.84 on-chip purity). The on-chip

https://doi.org/10.1038/s41566-026-01868-5

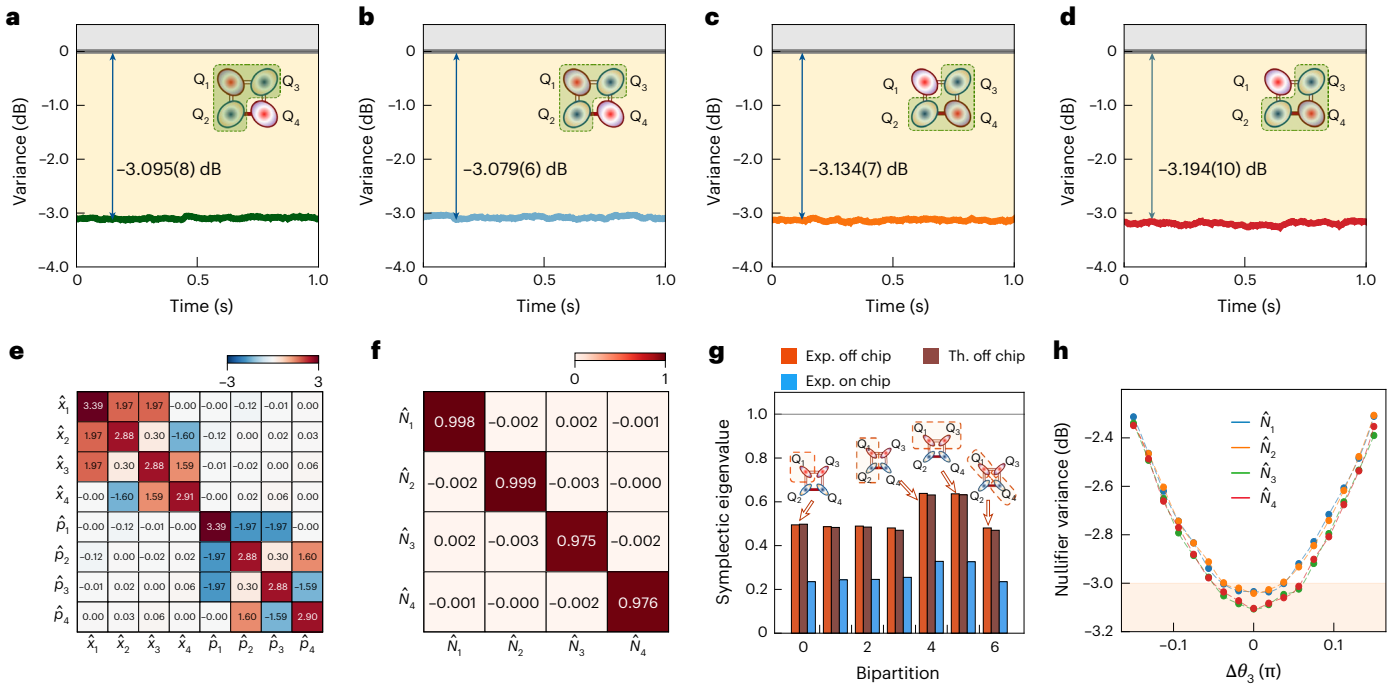


**Fig. 4 | On-chip generation and verification of four-qumode cluster-state entanglement. a**–**d**, Experimental measurement of nullifiers $\hat{N}_i$ for the four-qumode box cluster state, $i \in [1, 2, 3, 4]$. **a**, $\hat{N}_1$. **b**, $\hat{N}_2$. **c**, $\hat{N}_3$. **d**, $\hat{N}_4$. The measured nullifiers $\hat{N}_i$ are shown next to the blue arrows with the values in parentheses indicating the $\pm1\sigma$ uncertainty, each estimated from a complete set of 400 data points. The grey regions above the short noise represent the absence of squeezing, while the orange regions represent the presence of strong squeezing. The grey horizonal lines (at 0 dB) indicate the nullifier variances when all qumodes are in the vacuum state, which is twice the single-qumode vacuum and corresponds to a value of 2 in equation (2). The inset diagrams represent the cluster structure of the four-qumode box-type cluster state. Each elliptic structure represents a squeezed qumode ($Q_1$–$Q_4$), the colours of which represent the non-degenerate frequency qumodes. White lines represent edges with $1/\sqrt{2}$ weight, and the red line represents an edge with $-1/\sqrt{2}$ weight. **e**, Experimentally reconstructed covariance matrix for the box cluster state measured by Gaussian state tomography. **f**, Experimentally reconstructed nullifier covariance matrix based on experimental results in **e**. The diagonal elements, representing individual nullifier variances, show strong agreement with the direct measurements in **a**–**d**. Near-zero off-diagonal elements confirm the unambiguous box-type cluster-state entanglement structure. **g**, The minimum symplectic eigenvalues of the partial transposed states all violate the separable bound of 1, proving full inseparability according to positive partial transpose criterion. Bipartitions include the first four 1|3 splits and the last three 2|2 splits. Insets: qumodes circled by dashed rectangles represent one part under bipartition 0, 4, 5, 6, respectively. **h**, Characterizations of entanglement robustness under phase noise. Points are experimental results and dashed lines connect data points for visual emphasis. The violation of van Loock–Furusawa criteria (orange region) persists when controlled phase noise is applied to the rotation gates $R(\theta_3)$. The full dataset is reported in Supplementary Fig. 6. Experimental data were collected at a 5 MHz sideband frequency.

purity of the cluster state was estimated to be 0.29 based on the reconstructed covariance matrix in Supplementary Fig. 7c. However, high-purity states are to create Schrödinger cat states and Gottesman–Kitaev–Preskill qubits[51–54]. We configured the DMDI sources to generate states with high purity at a squeezing level of −1.31 dB (equivalent to −2.5 dB on chip), a typical operating point for cat-state generation[53]. Figure 2d shows the measured state purity (on chip). Substantial enhancements in state purity were observed, such as achieving high purities of 0.91 (single-mode) and 0.99 (two-mode) for an escape efficiency of 0.95. The purity of the squeezed states can be estimated from $1/\sqrt{V_s V_a}$, where $V_s$ ($V_a$) denotes maximally squeezed (anti-squeezed) quadrature variance[55]. Note that in the single-ring sources, the purity for the single-mode squeezer could be diminished due to the presence of undesired non-degenerate FWM and Bragg-scattering FWM. The squeezed mode becomes entangled with other sideband modes, leading to a thermal state when tracing out those modes. To produce pure single-mode squeezing at the $\lambda_0$ mode, mode splitting at the $\lambda_{\pm2}$ modes (the subscript here represents the number of resonant modes) has been implemented to suppress these unwanted FWM processes[47]. The mechanism for this improvement in purity is described in Supplementary Section 2.2.3 and Supplementary Fig. 5. In our experiments, we used the auxiliary microring to shift the $\lambda_{\pm2}$ modes by at least 1.2 GHz (Supplementary Fig. 3), attaining a high purity of 0.91.

## Conclusion

In summary, we have demonstrated a monolithic integrated CV-QPIC that is capable of the on-chip generation, operation, measurement and verification of four-qumode spatial-multiplexed cluster states and offers deterministic entanglement and high-fidelity controllability. Although our current work remains at the level of small-scale entanglement, it not only rigorously realizes genuine multipartite entanglement with well-defined cluster-state structures, but also demonstrates the crucial capabilities necessary for scaling up to large-scale entanglement while retaining controllability. As a result of monolithic integration of squeezers, gates, LOs and projectors, we demonstrate the capabilities of addressing, operating and measuring individual qumodes and multi-qumode cluster states with exceptional phase stability and high fidelity. All of the CV-QPIC devices, particularly the penguin-shaped squeezers that can compensate for wafer-scale fabrication inhomogeneities, allow very-large-scale integration through high-volume manufacturing in the silicon nitride platform. Embedding photodiodes in circuits[56] could directly enhance the measurable squeezing and scale up the number of qumodes. The multiplexing of spatially encoded cluster states with frequency- or time-encoded states[9–12], for example, by leveraging a broad spectrum of frequency qumodes in larger microresonators[41] or a sequence of temporal qumodes in optical fibre delays[42], or even ultra-low-loss waveguides, could enable very-large-scale entanglement of light on photonic chips. A discussion on scaling the number

of entangled qumodes is provided in Supplementary Section 4.4. Our reported CV-QPIC technology is also fully compatible with established DV-QPIC technologies[15] (see discussions of hybrid CV–DV integration in Supplementary Section 5). This compatibility opens a route towards the on-chip generation of non-Gaussian states such as cat states and Gottesman–Kitaev–Preskill qubits[51–54] via photon-number-resolving detection, for example, promising fault-tolerant, universal quantum computing with integrated optics.

## Online content

Any methods, additional references, Nature Portfolio reporting summaries, source data, extended data, supplementary information, acknowledgements, peer review information; details of author contributions and competing interests; and statements of data and code availability are available at https://doi.org/10.1038/s41566-026-01868-5.

## References


1. Zhong, H.-S. et al. Quantum computational advantage using photons. *Science* **370**, 1460–1463 (2020).
2. Arute, F., Arya, K., Babbush, R. et al. Quantum supremacy using a programmable superconducting processor. *Nature* **574**, 505–510 (2019).
3. Guo, S.-A. et al. A site-resolved two-dimensional quantum simulator with hundreds of trapped ions. *Nature* **630**, 613–618 (2024).
4. Bluvstein, D. et al. Logical quantum processor based on reconfigurable atom arrays. *Nature* **626**, 58–65 (2024).
5. O'Brien, J. L., Furusawa, A. & Vučković, J. Photonic quantum technologies. *Nat. Photon.* **3**, 687–695 (2009).
6. Raussendorf, R. & Briegel, H. J. A one-way quantum computer. *Phys. Rev. Lett.* **86**, 5188–5191 (2001).
7. Menicucci, N. C. et al. Universal quantum computation with continuous-variable cluster states. *Phys. Rev. Lett.* **97**, 110501 (2006).
8. Weedbrook, C. et al. Gaussian quantum information. *Rev. Mod. Phys.* **84**, 621–669 (2012).
9. Asavanant, W. et al. Generation of time-domain-multiplexed two-dimensional cluster state. *Science* **366**, 373–376 (2019).
10. Larsen, M. V. et al. Deterministic generation of a two-dimensional cluster state. *Science* **366**, 369–372 (2019).
11. Chen, M., Menicucci, N. C. & Pfister, O. Experimental realization of multipartite entanglement of 60 modes of a quantum optical frequency comb. *Phys. Rev. Lett.* **112**, 120505 (2014).
12. Roslund, J. et al. Wavelength-multiplexed quantum networks with ultrafast frequency combs. *Nat. Photon.* **8**, 109–112 (2014).
13. Yukawa, M., Ukai, R., van, L. P. & Furusawa, A. Experimental generation of four-mode continuous-variable cluster states. *Phys. Rev. A* **78**, 012301 (2008).
14. Su, X. et al. Gate sequence for continuous variable one-way quantum computation. *Nat. Commun.* **4**, 2828 (2013).
15. Wang, J., Sciarrino, F., Laing, A. & Thompson, M. G. Integrated photonic quantum technologies. *Nat. Photon.* **14**, 273–284 (2020).
16. Pelucchi, E. et al. The potential and global outlook of integrated photonics for quantum technologies. *Nat. Rev. Phys.* **4**, 194–208 (2022).
17. Senellart, P., Solomon, G. & White, A. High-performance semiconductor quantum-dot single-photon sources. *Nat. Nanotechnol.* **12**, 1026–1039 (2017).
18. Cheng, R. et al. A 100-pixel photon-number-resolving detector unveiling photon statistics. *Nat. Photon.* **17**, 112–119 (2023).
19. Alexander, K. et al. A manufacturable platform for photonic quantum computing. *Nature* **641**, 876–883 (2025).
20. Kues, M. et al. On-chip generation of high-dimensional entangled quantum states and their coherent control. *Nature* **546**, 622–626 (2017).
21. Wang, J. et al. Multidimensional quantum entanglement with large-scale integrated optics. *Science* **360**, 285–291 (2018).
22. Llewellyn, D. et al. Chip-to-chip quantum teleportation and multi-photon entanglement in silicon. *Nat. Phys.* **16**, 148–153 (2020).
23. Chen, S. et al. Heralded three-photon entanglement from a single-photon source on a photonic chip. *Phys. Rev. Lett.* **132**, 130603 (2024).
24. Pont, M. et al. High-fidelity four-photon GHZ states on chip. *npj Quantum Inf.* **10**, 50 (2024).
25. Maring, N. et al. A versatile single-photon-based quantum computing platform. *Nat. Photon.* **18**, 603–609 (2024).
26. Bao, J. et al. Very-large-scale integrated quantum graph photonics. *Nat. Photon.* **17**, 573–581 (2023).
27. Huang, J. et al. Demonstration of hypergraph-state quantum information processing. *Nat. Commun.* **15**, 2601 (2024).
28. Zheng, Y. et al. Multichip multidimensional quantum networks with entanglement retrievability. *Science* **381**, 221–226 (2023).
29. Mondain, F. et al. Chip-based squeezing at a telecom wavelength. *Photon. Res.* **7**, A36–A39 (2019).
30. Nehra, R. et al. Few-cycle vacuum squeezing in nanophotonics. *Science* **377**, 1333–1337 (2022).
31. Stokowski, H. S. et al. Integrated quantum optical phase sensor in thin film lithium niobate. *Nat. Commun.* **14**, 3355 (2023).
32. Masada, G. et al. Continuous-variable entanglement on a chip. *Nat. Photon.* **9**, 316–319 (2015).
33. Lenzini, F. et al. Integrated photonic platform for quantum information with continuous variables. *Sci. Adv.* **4**, eaat9331 (2018).
34. Stefszky, M. et al. Waveguide cavity resonator as a source of optical squeezing. *Phys. Rev. Appl.* **7**, 044026 (2017).
35. Zhao, Y. et al. Near-degenerate quadrature-squeezed vacuum generation on a silicon-nitride chip. *Phys. Rev. Lett.* **124**, 193601 (2020).
36. Vaidya, V. D. et al. Broadband quadrature-squeezed vacuum and nonclassical photon number correlations from a nanophotonic device. *Sci. Adv.* **6**, eaba9186 (2020).
37. Yang, Z. et al. A squeezed quantum microcomb on a chip. *Nat. Commun.* **12**, 4781 (2021).
38. Guidry, M. A. et al. Quantum optics of soliton microcombs. *Nat. Photon.* **16**, 52–58 (2022).
39. Arrazola, J. M. et al. Quantum circuits with many photons on a programmable nanophotonic chip. *Nature* **591**, 54–60 (2021).
40. Paesani, S. et al. Generation and sampling of quantum states of light in a silicon chip. *Nat. Phys.* **15**, 925–929 (2019).
41. Jia, X. et al. Continuous-variable multipartite entanglement in an integrated microcomb. *Nature* **639**, 329–336 (2025).
42. Aghaee, R. H. et al. Scaling and networking a modular photonic quantum computer. *Nature* **638**, 912–919 (2025).
43. Moss, D. J., Morandotti, R., Gaeta, A. L. & Lipson, M. New CMOS-compatible platforms based on silicon nitride and Hydex for nonlinear optics. *Nat. Photon.* **7**, 597–607 (2013).
44. Barbarossa, G., Matteo, A. M. & Armenise, M. N. Theoretical analysis of triple-coupler ring-based optical guided-wave resonator. *J. Lightwave Technol.* **13**, 148–157 (1995).
45. Tison, C. C. et al. Path to increasing the coincidence efficiency of integrated resonant photon sources. *Opt. Express* **25**, 33088 (2017).
46. Ji, Q.-X. et al. Multimodality integrated microresonators using the Moiré speedup effect. *Science* **383**, 1080–1083 (2024).
47. Zhang, Y. et al. Squeezed light from a nanophotonic molecule. *Nat. Commun.* **12**, 2233 (2021).

48. Menicucci, N. C., Flammia, S. T. & van, L. P. Graphical calculus for Gaussian pure states. *Phys. Rev. A* **83**, 042335 (2011).
49. van, L. P. & Furusawa, A. Detecting genuine multipartite continuous-variable entanglement. *Phys. Rev. A* **67**, 052315 (2003).
50. Adesso, G., Serafini, A. & Illuminati, F. Extremal entanglement and mixedness in continuous variable systems. *Phys. Rev. A* **70**, 022318 (2004).
51. Ourjoumtsev, A., Tualle-Brouri, R., Laurat, J. & Grangier, P. Generating optical Schrödinger kittens for quantum information processing. *Science* **312**, 83–86 (2006).
52. Ourjoumtsev, A., Jeong, H., Tualle-Brouri, R. & Grangier, P. Generation of optical 'Schrödinger cats' from photon number states. *Nature* **448**, 784–786 (2007).
53. Konno, S. et al. Logical states for fault-tolerant quantum computation with propagating light. *Science* **383**, 289–293 (2024).
54. Larsen, M. V. et al. Integrated photonic source of Gottesman–Kitaev–Preskill qubits. *Nature* **642**, 587–591 (2025).
55. Paris, M. G. A., Illuminati, F., Serafini, A. & De, S. S. Purity of Gaussian states: measurement schemes and time evolution in noisy channels. *Phys. Rev. A* **68**, 012314 (2003).
56. Tasker, J. F. et al. Silicon photonics interfaced with integrated electronics for 9 GHz measurement of squeezed light. *Nat. Photon.* **15**, 11–15 (2021).

**Publisher's note** Springer Nature remains neutral with regard to jurisdictional claims in published maps and institutional affiliations.

Springer Nature or its licensor (e.g. a society or other partner) holds exclusive rights to this article under a publishing agreement with the author(s) or other rightsholder(s); author self-archiving of the accepted manuscript version of this article is solely governed by the terms of such publishing agreement and applicable law.

© The Author(s), under exclusive licence to Springer Nature Limited 2026

## Data availability

The data that support the findings of this study are available from the corresponding authors.

## Acknowledgements

We acknowledge support from the National Natural Science Foundation of China (grant nos. 12325410, 62235001, 11834010, 123B2065, 124B2081 and 62505005), the Innovation Program for Quantum Science and Technology (grant nos. 2021ZD0301500 and 2024ZD0302401), the Beijing Natural Science Foundation (Z220008), the China National Postdoctoral Program for Innovative Talents (grant nos. BX20250180 and BX20240025), the China Postdoctoral Science Foundation (grant no. 2024M760071), the Fundamental Research Program of Shanxi Province (grant no. 20210302121002) and the Fund for Shanxi '1331 Project' Key Subjects Construction.

## Author contributions

X.J. and J.W. conceived the project. X.J., C.Z. and X.Z. designed the devices. X.J., C.Y., C.Z., X.Z., Y.Z., T.D. and Z.F. implemented the experiments. X.J., C.Y. and C.Z. provided the simulations and performed the theoretical analysis. X.S., Q.G. and J.W. managed the project. X.J., C.Y., C.Z. and J.W. wrote the manuscript with input from all authors. All authors discussed the results and contributed to the manuscript.

## Competing interests

The authors declare no competing interests.

## Additional information

**Supplementary information** The online version contains supplementary material available at https://doi.org/10.1038/s41566-026-01868-5.

**Correspondence and requests for materials** should be addressed to Xinyu Jia, Xiaolong Su or Jianwei Wang.

**Peer review information** *Nature Photonics* thanks Andrea Crespi, Craig Hamilton and Nicholas Harris for their contribution to the peer review of this work.

**Reprints and permissions information** is available at www.nature.com/reprints.